ELSEVIER

Contents lists available at ScienceDirect

# Journal of Ionic Liquids

journal homepage: www.elsevier.com/locate/jil



# B/N-doped carbon sheets from a new ionic liquid with excellent sorption properties for methylene blue



Julian Mehler<sup>a</sup>, Matthias Ermer<sup>b</sup>, Ulrike Paap<sup>c</sup>, Bettina S.J. Heller<sup>c</sup>, Florian Maier<sup>c</sup>, Hans-Peter Steinrück<sup>c</sup>, Martin Hartmann<sup>b</sup>, Carsten Korte<sup>d</sup>, Peter S. Schulz<sup>a,\*</sup>, Peter Wasserscheid<sup>a,e</sup>

- <sup>a</sup> Institute of Chemical Reaction Engineering, Friedrich-Alexander University Erlangen-Nürnberg, 91058 Erlangen, Germany
- <sup>b</sup> Erlangen Center for Interface Research and Catalysis (ECRC), Friedrich-Alexander University Erlangen-Nürnberg, 91058, Erlangen, Germany
- <sup>c</sup> Chair of Physical Chemistry II, Friedrich-Alexander-University Erlangen-Nürnberg, 91058 Erlangen, Germany
- <sup>d</sup> Forschungszentrum Jülich, Institute of Energy and Climate Research Fuel Cells (IEK-14), 52425 Jülich, Germany
- e Forschungszentrum Jülich, Helmholtz-Institute Erlangen-Nürnberg for Renewable Energy (IEK 11), 91058 Erlangen, Germany

#### ARTICLE INFO

#### ABSTRACT

Keywords:
Material synthesis
Ionic liquid precursor
B/N doped carbon nanosheets
Adsorption

The pyrolytic treatment of the novel ionic liquid 1-ethyl-3-methyl-imidazolium tetrakis-(1-imidazolyl)borate ([EMIM][BIm<sub>4</sub>]) allowed the preparation of B/N-doped carbonaceous materials with an exceptional performance in the adsorptive removal of the cationic dye methylene blue (MB) from wastewater. [EMIM][BIm<sub>4</sub>] was prepared via an easy and scalable synthesis protocol in very good yield. The carbon materials obtained after salt templated pyrolysis of the IL displayed high degrees of heteroatom doping (up to 22 wt% N, 3 wt% B) and high surface areas of up to 1860 m<sup>2</sup> g<sup>-1</sup>. The materials were tested for their performance in the adsorptive removal of MB from contaminated water. Adsorption equilibrium experiments revealed an adsorption capacity exceeding

 $500~{\rm mg~g^{-1}}$ , which is, to the best of our knowledge, the highest value reported so far. Time-resolved adsorption experiments showed that the materials not only exhibit high capacity but also very fast adsorption kinetics. Complete decolorization of MB solutions in only 5 min at high MB concentrations of  $100~{\rm mg~L^{-1}}$  was observed. These results demonstrate that [EMIM][BIm<sub>4</sub>] is an excellent precursor for the preparation of IL-derived B/N-doped carbon sorbents.

#### 1. Introduction

Due to their tunability, high surface area and stability, heteroatom-doped porous carbons have become a very interesting material class. In addition to their adsorptive properties, they have shown great potential in catalysis, energy conversion, energy storage, and sensing technologies. (Titirici et al., 2015, Su et al., 2013, Zhao et al., 2019, Jariwala et al., 2013, Liang et al., 2008) In most cases, their preparation is carried out *via* chemical vapor deposition (CVD) or *via* pyrolysis of an organic precursor. A wide choice of precursors has been found suitable, ranging from simple organic molecules like acetonitrile or melamine (Pacuła et al., 2016, Mombeshora et al., 2017, Yao et al., 2015), to polymers (Paraknowitsch et al., 2011), mixtures of organic salts (Luo et al., 2020), bio-based heterocycles (Yang et al., 2015), human hair (Chaudhari et al., 2014) or chicken feathers (Gao et al., 2014). Chemists have pyrolysed virtually everything in the search for new doped carbon materials!

A very popular class of pyrolysis precursors are ionic liquids (ILs). Their thermal stability and low volatility provide high yield during carbonization. Furthermore, the wide variety of possible cationanion combinations allows for control over the amount and nature of doped heteroatoms in the product. (Paraknowitsch and Thomas, 2012, Zhang et al., 2015) For the preparation of heteroatom-doped carbon materials from ILs, there are two general *modi operandi*, as the pyrolysis of neat, non-functionalized ILs still leads to decomposition and evaporation of the decomposition products.

In the first approach, the nano-confinement or templating approach, the ionic liquid is entrapped inside a porous support like silica. Mixing the IL with an inorganic salt prior to pyrolysis allows for the preparation of carbonaceous materials from ILs that would normally just decompose and evaporate under pyrolysis conditions, such as [BMIM][NTf $_2$ ] or [EMIM]Br. (Wang and Dai, 2010, Chen et al., 2013, Zhang et al., 2017) Generally, after pyrolysis, a carbon material that is a structural 'negative' of the inorganic template is obtained. This allows for a more

E-mail address: peter.schulz@fau.de (P.S. Schulz).

Corresponding author.

Journal of Ionic Liquids 1 (2021) 100004

targeted approach towards the final product, as pore and structure engineering is possible through selection of the inorganic template.

The second pathway from ILs to doped carbon materials is prefunctionalization. The incorporation of cross-linkable nitrile groups at the IL cation or anion allows for the preparation of highly nitrogenenriched, porous carbons via pyrolysis of the neat IL. It is generally understood that these functionalities undergo polymerization and condensation reactions at elevated temperatures, resulting in a thermally stable resin that carbonizes with minimal loss of small, volatile organic molecules. (Fellinger et al., 2012), (Lee et al., 2009) Cations with nitrile functionalities can be prepared *via* quaternization reactions of imidazole with chloroacetonitrile or chlorobutyronitrile, whereas suitable nitrilebearing anions are dicyanamide [DCA] or tricyanomethanide [TCM]. (Prechtl et al., 2009, Drab et al., 2012, Kuzmina et al., 2017, Zhu et al., 2012) Thus with the structural variation of cation and anion of the IL, the composition of the carbon materials and their heteroatom content can be controlled. Nitrogen as a dopant is relatively straightforward to achieve, as, for example, the nitrogen content of the popular 1ethyl-2-methylimidazolium cation ([EMIM]+), is already approximately 25 wt%. This cation paired with a [DCA] ion gives almost 40 wt% of N in the precursor IL, which allows for the preparation of highly N-doped carbon materials. Antonietti et al. reported that the material obtained after SBA-15 templated pyrolysis of [EMIM][DCA] at 1000°C still contained 10.4 wt% of nitrogen. (Paraknowitsch et al., 2010) If not only N but also S is desired in the product, the bistriflimide ([NTf<sub>2</sub>]<sup>-</sup>) anion can be used instead of [DCA]-. Leung et al. used [BMIM][NTf<sub>2</sub>] as an IL-precursor in a graphite-templated pyrolysis at 900°C. The product not only had high nitrogen content (up to 13 at%), but also incorporated sulphur (up to 0.5 at%) in the final product. (She et al., 2015) The pyrolysis of neat mixtures of [DCA] and [NTf2]-ILs was investigated by Kim et al.. [EMIM][DCA] was chosen as the carbonization agent, trapping the bulky [NTf2] ions inside the polymerized carbon matrix. Subsequent thermal decomposition of [NTf<sub>2</sub>]<sup>-</sup> then led to pore formation without the use of any additional inorganic template. A high N content (16.1 at%), as well as S (0.6 at%) and F (0.3 at%) doping, paired with a high specific surface area of 625 m<sup>2</sup> g<sup>-1</sup> was obtained after pyrolysis at 900°C. (Jeong et al., 2017) Mixing [DCA]--ILs with phosphonium ILs and subsequent pyrolysis opens the pathway to N and P co-doped materials, as shown by Thomas et al.. (Paraknowitsch et al., 2013) Dissolving tetrabutylphosphonium bromide in 1-butyl-3-methylpyridinium [DCA] yielded carbon materials with up to 5.7 wt% of P and 4.1 wt% of N after pyrolysis at 1000°C.

Another popular dopant for carbon materials is boron. When paired with nitrogen, B- and N-doped carbons (BNCs) are formed that offer most interesting materials properties for applications in electrocatalysis, sensing and adsorption. (Panchakarla et al., 2009, Inagaki et al., 2018, Abbas et al., 2019, Gouse Peera et al., 2020, Han et al., 2020) Interestingly, among the ions commonly used in the field of IL chemistry, there are only two containing boron, tetrafluoroborate [BF4] and tetracyano-borate [TCB]. Although [BF4] has been used in the preparation of B-doped carbons, its use as a precursor is hampered by the formation of gaseous HF during pyrolysis. (Chen et al., 2016), (Ohtani et al., 2008) Despite the formation of HCN during pyrolysis, [TCB]-ILs proved the more popular choice as a precursor IL, most likely due to the nitrile functionality in the anion, that allows for fast network formation under thermal treatment and leads to a very effective formation of BNCs. (Paraknowitsch and Thomas, 2017, Fulvio et al., 2011, Aijaz et al., 2014, Ranjbar Sahraie et al., 2014) A drawback of using [TCB]--ILs, however, is their very limited commercial availability nowadays. (SciFinder®, 2014) The synthesis of [TCB]<sup>-</sup>-ILs relies on the rather unpleasant preparation of K[TCB] which uses an excess of molten KCN and gives relatively low yields after tedious work-up procedures. (Bernhardt et al., 2003) Here, we want to introduce an alternative anion that, to the best of our knowledge, has not yet been explored in the context of ILs, tetrakis(1-imidazolyl)borate ([BIm<sub>4</sub>]<sup>-</sup>). So far, [BIm<sub>4</sub>]<sup>-</sup> was mostly used by the metal-organic-frameworks community as a linker for the preparation of lightweight porous materials. (Zhang et al., 2010, Galvelis et al., 2012, Zheng et al., 2010) With the central boron atom and four imidazolyl wings, [BIm<sub>4</sub>] - strongly resembles [TCB] - and can be used as an alternative in the pyrolytic preparation of BNCs. In this manuscript we present a synthesis protocol for the preparation of Na[BIm<sub>4</sub>] in larger scale (up to 200 g per batch), and starting from this salt, the detailed synthesis of the new IL [EMIM][BIm4] is reported. After the purity of the IL was confirmed, the salt was applied as a precursor in the preparation of B- and N-doped carbon materials, resulting in high degrees of heteroatom doping (up to 22 wt% N, 3 wt% B) and high surface area materials (up to 1860 m (Su et al., 2013)  $\rm g^{-1}$  internal surface). After materials characterization by elemental analysis, ICP-OES, gas sorption, IR spectroscopy, RAMAN spectroscopy, X-ray induced photoelectron spectroscopy, XRD and microscopy, the materials were tested in the adsorptive removal of the pollutant methylene blue (MB). Excellent performance, with an uptake of 0.25 g of MB per gram of BNC in 5 min and a maximum capacity of over 500 mg g<sup>-1</sup> was found. This is, to the best of our knowledge, the highest value for this class of materials reported so far. Our study provides not only an alternative to TCB--ILs for the preparation of BNCs but also shows the potential of the new [BIm<sub>4</sub>]-ILs as versatile precursor in the field of material synthesis.

#### 2. Experimental details

#### 2.1. Chemicals

All regular solvents and chemicals were purchased from commercial suppliers and were of reagent grade. Unless otherwise stated, all chemicals were used as received. Sodium borohydride (≥ 98 %, granular form) was purchased from Merck. Imidazole (99 %) was purchased from Alfa Aesar. 1-Ethyl-3-methylimidazolium chloride ([EMIM]Cl, >98 %) was purchased from Iolitec and recrystallized from ethyl acetate/acetonitrile 7:1 v:v, dried *in vacuo* and stored under argon, prior to the reaction.

# 2.2. Synthetic procedures

#### 2.2.1. Synthesis of sodium tetrakis-(1-imidazolyl)borate

Na[BIm<sub>4</sub>] was synthesized *via* an up-scaled synthesis procedure, originally published by Hamilton *et al.* and

Chao et al. (Chao and Moore, 1978; Hamilton et al., 2003) Under a constant flow of argon, a 1 l glass reactor (for a detailed flowchart see Fig. S1) was charged with imidazole (360 g, 5.287 mol, 8 eq.). The reaction temperature was set to 110°C and imidazole was molten under slow stirring (300 rpm), over the course of 30 min. As soon as the imidazole liquefied, the reaction temperature was slowly raised to 225°C and simultaneously Na[BH<sub>4</sub>] (25 g, 0.661 mol, 1 eq) was added in small portions via a lab-scale snail extruder. Vigorous evolution of H<sub>2</sub> was observed, as the Na[BH4] granules reacted with the molten imidazole.† Upon complete addition, the reaction mixture was stirred at 225°C for an additional 3 h, to guarantee full conversion of Na[BH<sub>4</sub>]. The heating mantle was removed and the reaction mixture was cooled down using a water bath. 800 mL of acetone were added slowly, during which an off-white crude-product precipitated. After filtration, the residue was washed with two portions of acetone (500 mL each), then with one portion of cold ethanol (250 mL). Drying in vacuo gave the product as a white powder (187 g, 0.619 mol, 93.64 %). Purity was confirmed via NMR spectroscopy and elemental analysis (EA, see ESI for details).

# 2.2.2. Synthesis of 1-ethyl-3-methylimidazolium tetrakis-(1-imidazolyl)-borate

[EMIM][BIm<sub>4</sub>] was synthesized *via* a simple salt metathesis reaction, starting from [EMIM]Cl and Na[BIm<sub>4</sub>]. A 500 mL two-necked flask, equipped with a magnetic stirring bar and a reflux condenser, was charged with Na[BIm<sub>4</sub>] (15.1 g, 50 mmol, 1 eq.) and 350 mL of ethanol as a solvent. The reaction mixture was heated to reflux under constant stirring (500 rpm) until Na[BIm<sub>4</sub>] dissolved completely. A clear solution

of [EMIM]Cl (7.33 g, 50 mmol, 1 eq) in 50 mL of ethanol was added in one portion. A white precipitate formed immediately and stirring was continued under reflux for 60 min. The reaction mixture was cooled down to room temperature, filtered and the residue was washed with three portions of cold ethanol (25 mL each). The solvent was removed under reduced pressure to give a solid, yellow crude-product. To remove residual traces of NaCl in the IL, the crude-product was taken up in hot 1-butanol (250 mL) and the solution was filtered again. After removal of 1-BuOH and drying in vacuo, [EMIM][BIm4] was obtained as a hygroscopic yellow solid (17.17 g, 44 mmol, 88 %, M= 390.26 g mol<sup>-1</sup>). Purity was confirmed via NMR spectroscopy and elemental analysis. The melting point (57°C) was determined via differential scanning calorimetry. Due to the m.p., no viscosity measurements were performed. The decomposition temperature (T<sub>Onset</sub>: 213°C) was determined via thermogravimetric analysis. Details can be found in the ESI. Until further processing, the product was stored under argon.

#### 2.3. Preparation and characterization of BNC materials

The BNC materials were synthesized from [EMIM][BIm4] using a salt-templating method, adapted from Fechler et al. (Fechler et al., 2013) In a 100 mL beaker, 16 g of [EMIM][BIm4] were combined with 48 g of a eutectic mixture of ZnCl2 and NaCl (36.63 g and 11.37 g, respectively) that served as a porogen during pyrolysis. The IL/salt mixture was slowly heated to 80°C under gentle stirring to give a slightly yellow, homogenous paste. This precursor was transferred into porcelain crucibles and pyrolyzed at up to 1000°C in a Carbolyte CWF 1100 chamber oven under a constant stream of argon for 2 h and with a heating rate of 10 K min<sup>-1</sup>. The samples were allowed to cool down to room temperature, combined, ground in a mortar and washed with 200 mL of HCl (10 wt%) and NaOH (0.1 M), respectively, in two consecutive steps, for 1 h each. After filtration, the samples were washed with H<sub>2</sub>O until a neutral pH was achieved and dried in an oven at 100°C over night. The three samples prepared were denoted as BNC-800, BNC-900 and BNC-1000, with the number representing the respective pyrolysis temperature.

To determine the bulk elemental composition of BNC materials, elemental analysis (UNICUBE®, elementar) and ICP-OES (CIROS-CCD, SPECTRO) were used. For surface analysis and evaluation of chemical bonding, X-ray photoelectron spectroscopy (DASSA (Niedermaier et al., 2016), Omicron NanoTechnology, monochromated Al K<sub>a</sub> X-ray source, 1486.6 eV, 238 W, detection angle of 0° to the surface normal of the sample) and FTIR (FT/IR-4600, Jasco, KBr pellet) were used. The morphology was studied by SEM (ULTRA 55 SEM, Carl Zeiss) and TEM (CM 30, Philips). The specific surface area ( $S_{\mbox{\footnotesize BET}}$ ) was calculated by applying the Brunauer-Emmett-Teller (BET) model to N2 adsorption isotherm data points (ASAP 2000, Micromeritics). The pore size distribution was calculated using the NLDFT equilibrium model method for carbon slit pores. Powder X-ray diffraction patterns were collected on a Philips X'Pert Pro MPD diffractometer in Bragg-Brentano geometry equipped with a pixcel (Zhao et al., 2019)D line detector. The copper X-ray tube providing  $CuK\alpha_1$  ( $\lambda = 1.5406$  Å) radiation was operated at 40 kV and 40 mA. For Raman spectroscopy, an AvaRaman-532HERO-EVO (Avantes) system with an AvaRaman-PRB-532 (Avantes) probe was used. The Raman solution consisted of a 532 nm (green) solid state laser (Cobolt) and an AvaSpec-HERO (Avantes) spectrometer with a grating set of 1200 lines mm<sup>-1</sup> (HSC1200-0.75). The spectrometer was equipped with a 50 μm slit and the detected wavelength range was 534-696 nm. The Raman spectra were collected in 10 repetitions at 50 mW laser power with an exposure time of 10 s.

# 2.4. Adsorption kinetics of MB

In a typical time-resolved adsorption experiment, a 50 mL Schott bottle was charged with 20 mg of BNC adsorbent and 50 mL of MB solution ( $c_0=20~\text{mg}~\text{L}^{-1}$  or 100 mg L<sup>-1</sup>) were added under vigorous stirring

(800 rpm), to guarantee a homogeneous suspension. The recording time was started immediately upon addition of the solution and samples of 2.5 mL were withdrawn either every minute (for BNC-800 at  $c_0=100~\rm mg~L^{-1}$ ), or every 30 s (for BNC-900 and BNC-1000). After filtration using a 0.45  $\mu m$  PTFE syringe filter, the remaining concentration of MB in solution (ct) was measured using a UV/Vis spectrometer (Specord 205, Analytic Jena), calibrated at 663 nm. From ct the amount of adsorbed MB at time-interval t (qt) could then be calculated using:

$$q_t = \frac{V(c_0 - c_t)}{m} \tag{1}$$

where V (l) is the volume of the MB solution,  $c_0$  (mg  $L^{-1}$ ) is the initial concentration of MB and m (g) is the mass of the BNC adsorbent.

#### 2.5. Adsorption capacity and isotherms

Stock solutions of MB (50 mg  $L^{-1}$  up to 400 mg  $L^{-1}$ ) were prepared by dissolving the respective amount of MB in 1 L of deionized  $\rm H_2O$  and used without further pH correction. In a typical equilibration experiment, 10 mg of BNC adsorbent were mixed with 25 mL of MB stock solution and vigorously stirred for 24 h at room temperature. A sample of 3 mL was withdrawn and filtered using a 0.45  $\mu m$  PTFE syringe filter. The remaining concentration of MB at equilibrium (ce) was then measured using a UV/Vis spectrometer (Specord 205, Analytic Jena), calibrated at 663 nm. With ce, the adsorption capacity (qe) could then be calculated using the following equation:

$$q_e = \frac{V(c_0 - c_e)}{m} \tag{2}$$

where  $q_e$  (mg g  $^{-1})$  is the adsorption capacity at equilibrium, V (l) is the volume of the MB solution,  $c_0$  and  $c_e$ 

(mg  $L^{-1}$ ) are the initial and equilibrium concentration of MB, respectively and m (g) is the mass of the BNC adsorbent. To fit the values of  $q_e$  at different  $c_e$ , three adsorption isotherm models were used in this study. The Langmuir isotherm model is based on a monolayer sorption without interaction between sorbed molecules on the homogeneous surface. (Langmuir, 1918) The  $q_e$  value is determined by Equation 3.

$$q_e = \frac{q_{max} K_L c_e}{1 + K_L c_s} \tag{3}$$

with  $q_e$  (mg  $g^{-1}$ ) and  $c_e$  (mg  $L^{-1}$ ) being the adsorption capacity and concentration of adsorbate at equilibrium, respectively,  $q_{max}$  (mg  $g^{-1}$ ) is the theoretical maximum adsorption capacity with monolayer coverage and  $K_r$ 

(L mg<sup>-1</sup>) is the Langmuir isotherm constant, related to the favorability of adsorption. The Freundlich equation describes multilayer sorption on a heterogeneous surface (Equation 4). (Freundlich, 1907)

$$q_e = K_F \cdot c_e^{1/n} \tag{4}$$

 $\rm K_F$  and 1/n are constants related to adsorption capacity and intensity, respectively. The Brouers-Sotolongo isotherm model is based on statistical analysis of complex sorption processes and considers physical and chemical heterogeneities of the adsorbent and of the adsorbent/adsorbate system. (Brouers et al., 2005, Ncibi et al., 2008, Altenor et al., 2009) The Brouers-Sotolongo isotherm (BSI) is calculated according to Equation 5.

$$q_e = q_{max} \left( 1 - e^{\left( -K_W c_e^{\alpha} \right)} \right) \tag{5}$$

with  $K_W = K_F/q_{max}$ , where  $K_F$  is the Freundlich constant at low  $c_e$  and  $\alpha$  is a measure of the energy heterogeneity of the sorbent surface.

#### 2.6. Influence of pH on adsorption capacity

HCl (10 wt%) and NaOH (0.1 M) were used to prepare five solutions with a pH value of 2, 4, 6, 8 and 10. To these solutions, an appropriate amount of MB was added, to give an initial concentration of MB of 100 mg  $\rm L^{-1}$ . To determine the adsorption capacity of BNC-1000 at varying

pH value, 10 mg of adsorbent were mixed with 50 mL of previously prepared stock solutions and vigorously stirred for 24 h. A sample of 3 mL was withdrawn and filtered using a 0.45  $\mu$ m PTFE syringe filter. Using UV/Vis,  $c_e$  was measured and  $q_e$  was calculated (*vide supra*).

#### 3. Results and discussion

#### 3.1. Material synthesis

Due to the need for larger quantities of Na[BIm4] in this study, an up-scaled synthesis protocol was developed that produces almost 200 g of Na[BIm<sub>4</sub>] in high purity in one batch. The procedures reported in literature so far, (Chao and Moore, 1978; Hamilton et al., 2003) describe charging a flask with Na[BH4] and an excess of imidazole, then heating the reaction mixture until H2 evolution ceases. This formation of gaseous co-product raises severe safety concerns in larger batches, as per gram of Na[BH<sub>4</sub>], over 2 L of flammable hydrogen gas are produced. To allow for better reaction control, in this study a fed-batch operation mode was employed, where small portions of Na[BH₄] are continuously fed into molten imidazole at elevated temperatures. As opening the reactor and manual addition of borohydride leads to loss of imidazole, a lab-scale snail extruder was used instead, which guarantees continuous addition of reagent in a closed environment. After purification, the product Na[BIm4] is obtained in high purity and almost quantitative vield.

For the preparation of the IL [EMIM][BIm<sub>4</sub>], a common salt-metathesis with Na[BIm<sub>4</sub>] and [EMIM]Cl in EtOH was used (precipitation of NaCl). As with most ILs prepared via this method, a residual NaCl impurity was detected in the elemental analysis after this step. For further purification, the crude product was dissolved in hot 1-BuOH and insoluble NaCl was removed via filtration. Interestingly, the use of n-butanol proved crucial in this step, as more polar solvents, like isopropanol, do not lead to the precipitation of NaCl. Less polar solvents, like acetonitrile, on the other hand, also precipitate traces of Na[BIm<sub>4</sub>] and this leads to an excess of [EMIM]Cl in solution. After drying [EMIM][BIm<sub>4</sub>] in vacuo, the absence of NaCl was confirmed by elemental analysis. Furthermore,  $^1$ H-NMR spectroscopy showed an [EMIM] to [BIm<sub>4</sub>] ratio of 1:1 and confirmed the absence of organic impurities.

For the preparation of the porous BNC adsorbent materials from [EMIM][BIm $_4$ ], a salt-templating method, originally published by Fechler *et al.* (Fechler et al., 2013; Fechler et al., 2014) was used. An eutectic mixture of NaCl and ZnCl $_2$  served as the porogen. This approach was necessary as pyrolysis of pure [EMIM][BIm $_4$ ] only yielded non-porous materials. This result is not surprising, as literature suggests a need for polymerizable nitrile functionalities on either the IL cation or the IL anion for self-templating processes towards porous pyrolysis products. (Paraknowitsch and Thomas, 2012; Zhang et al., 2015) [EMIM][BIm $_4$ ] obviously lacks those functionalities and therefore the IL requires external templating.

In a first step, the IL was simply mixed with the salts in a beaker under elevated temperatures until a homogeneous paste was obtained. This IL/template mixture was transferred to porcelain crucibles and pyrolyzed under inert gas. During pyrolysis, the eutectic mixture of inorganic salts melts and forms an inorganic matrix. This matrix mixes with the organic IL to give heteroatom-doped carbons under pyrolysis conditions. After carbonization, the template was removed with dilute HCl, NaOH and  $\rm H_2O$ . All materials were obtained as shiny black powders in mass yields of approximately 35%.

#### 3.2. Material characterization

The bulk elemental analyses (EA & ICP) of BNCs are summarized in Table 1. Interestingly, EA also detected hydrogen and oxygen. Because these values closely match the stoichiometry of water and only insignificant amounts of oxygen bonds were found by other analytic methods

**Table 1**Bulk elemental composition in wt% and sum formula of BNC materials prepared in this study.

Sample	C (wt%)	C (wt%) N (wt%)		Sum formula <sup>a</sup>	H, O (wt%)b	
BNC-800 BNC-900	53.4 68.3	21.7 12.0	2.8 1.6	C <sub>17</sub> N <sub>6</sub> B C <sub>38</sub> N <sub>5</sub> B	2.6, 19.5 2.0, 16.1	
BNC-1000	74.7	8.2	2.1	$C_{38}N_5B$ $C_{32}N_3B$	1.7, 13.3	

<sup>&</sup>lt;sup>a</sup> calculated from bulk elemental analysis, rounded to full integers and normalized to boron <sup>b</sup> attributed to adsorbed water, included for completeness.

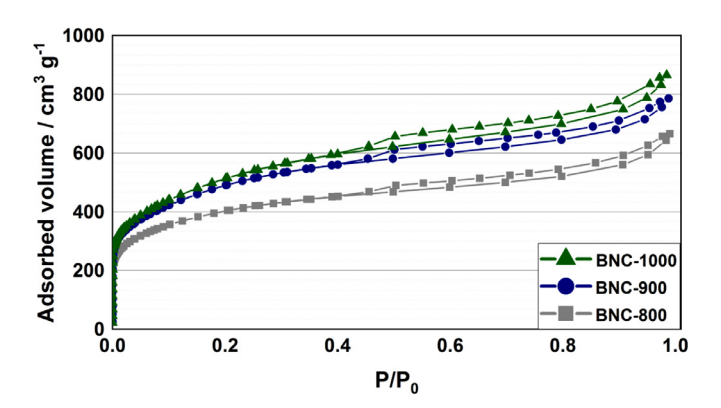


Fig. 1. N<sub>2</sub> sorption isotherms of BNCs pyrolyzed at different temperatures.

(vide infra), these amounts were mainly attributed to adsorbed water on the surface of the porous samples.

Generally, all samples show a high degree of N and B doping, with a decrease in doping with higher pyrolysis temperatures. With an increase of temperature, only a small change in absolute boron content can be observed, whereas nitrogen drastically decreases and carbon increases. This result is in accordance with investigations on the pyrolysis of tetracyanoborate-ILs by Fellinger et al. (Fellinger et al., 2012) At temperatures close to 1000°C, the thermodynamically stable B-N bond stabilizes nitrogen bonded to boron, while imidazole units undergo rearrangements and cross-linking reactions towards carbonaceous materials. Nitrogen bonded exclusively to carbon can be lost as HCN or alkylcyanides during this process and this reduces N doping in the final material. Remarkably, even BNC-1000 still contains more than 10 wt% of heteroatoms in its structure, which is one of the highest degrees of doping for a B/N-doped porous carbon material reported so far (see Castro-Muñiz et al. (Castro-Muñiz et al., 2017), and references therein). Furthermore, as [BIm<sub>4</sub>] inherently provides only B-N bonds, no boron bound to carbon is expected in our BNC materials.

Nitrogen sorption/desorption experiment were conducted to investigate the porous structure of BNCs and these are depicted in Fig. 1. The specific surface areas are generally very high and materials pyrolyzed at higher temperatures show a higher  $S_{BET}$  (BNC-800, 1470  $\rm m^2~g^{-1}$ , BNC-900, 1788  $\rm m^2~g^{-1}$ ). It is worth noting that BNC-1000 (1860  $\rm m^2~g^{-1}$ ) approaches the maximum theoretical  $S_{BET}$  of single-layer graphene sheets (2000  $\rm m^2~g^{-1}$ ). (Rao et al., 2009) As can be seen, all three materials show type I(b) isotherms, typical for materials with a wide pore size distribution in the micropore and narrow mesopore region. (Thommes et al., 2015) The observed hysteresis can be attributed to interparticle condensation. Specifically the sharp uptake in the low pressure region implies numerous micropores, which is confirmed by the pore size distributions (see Fig. S2). All BNCs display a porous network of small mesopores

 $(<4~\rm nm)$  and micropores. Interestingly, although BNC-1000 has the highest  $S_{\rm BET},$  it has the lowest relative amount of micropores  $<1~\rm nm,$  which indicates continuous burn-off during pyrolysis, resulting in an increasing amount of micro and small mesopores, as well as an increase in specific surface area.

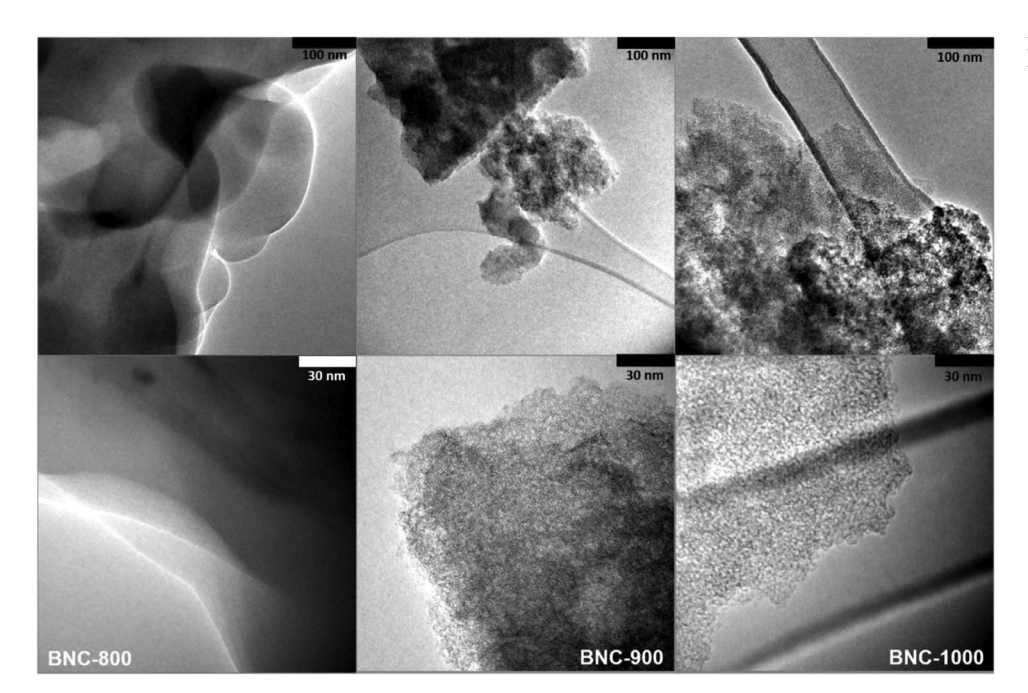


**Fig. 2.** TEM pictures of BNC-800 (left column), BNC-900 (middle column) and BNC-1000 (right column).

This burn-off is also observed in electron microscopy. Although the materials looked relatively similar in SEM pictures (see Fig. S3), the TEM pictures revealed significant differences in morphology, as depicted in Fig. 2. Where BNC-800 shows a 2D structure of smooth, overlapping nanosheets, BNC-900 and BNC-1000 display increasing roughness on their surface with a porous texture clearly visible. This increasing amount of defects (or holes in the sheet) originates from the evaporation of ZnCl<sub>2</sub> and volatile organic molecules at elevated temperatures and is most likely the reason for the higher specific surface areas of BNC-900 and BNC-1000, when compared to BNC-800.

To investigate crystallinity of BNCs, Raman spectra were recorded (see Fig. S4). Two dominant bands can be observed. The relatively broad D band at approx. 1355 cm<sup>-1</sup> is assigned to asymmetric B-N domains and defective graphite. The G-band at approximately 1590 cm<sup>-1</sup> is assigned to sp<sup>2</sup>-hybridised graphite-like structures. (Lazzarini et al., 2016, Tuinstra and Koenig, 1970, Ferrari and Robertson, 2000) Integration using a lorentzian line shape of both bands allows for a comparison of disordered and ordered (ergo crystalline) domains in the material by dividing the D-band area by the G-band area (ID/IG). Following this, a perfect graphene sheet would have a I<sub>D</sub>/I<sub>G</sub> ratio of 0, as no D-band would be measurable. BNC-1000 shows the lowest  $I_D/I_G$  ratio with 1.14, which is a sign for higher degree of graphitization and crystallinity than in BNC-900 ( $I_D/I_G=1.27$ ) and BNC-800 ( $I_D/I_G=1.41$ ). This implies that higher pyrolysis temperatures (close to 1000°C) favor the burn-off of rather volatile, amorphous structures and promote the formation of sp<sup>2</sup>-hybridized, aromatic architectures. This observation was confirmed with XRD measurements (see Fig. S5). All three materials show two broad diffractions at 25°, corresponding to the graphite (002) plane, and at 44°, corresponding to the graphite (100) plane. Interestingly, the diffraction pattern at 25° broadens with increasing pyrolysis temperature, indicating a decrease in stacking order of BNC-sheets. In contrast, the diffraction pattern at 44° becomes more pronounced and narrow at higher temperatures. Hence, while vertical order decreases, an increase in lateral, in-plane order is observed. This shows that, although the stacking of BNC-sheets is more turbostratic at higher pyrolysis temperatures, the sheets per se have a more crystalline character.

To investigate chemical bonding in the bulk material, FTIR spectra were recorded (see Fig. 3). The sharp peak at 1380  $\rm cm^{-1}$  is assigned to in-plane vibrations of  $\rm sp^2$ -bonded boron nitride. The relatively broad band at

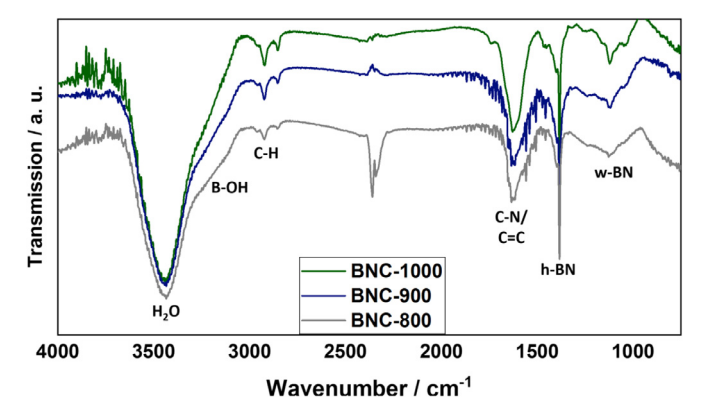
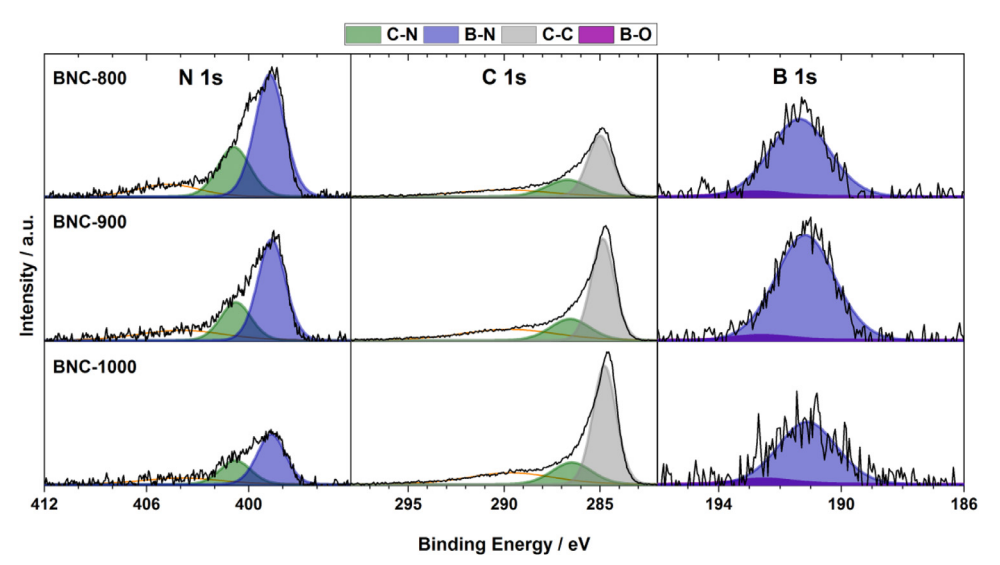


Fig. 3. FTIR spectra of BNC materials pyrolyzed at different temperatures.

1620 cm<sup>-1</sup> can be ascribed to C=C and C-N stretching vibrations of the graphitic domains, nitrogen-doped in the graphitic phase and the frontier from graphitic to boron nitride domains, respectively. Both signals show that BNCs consist of a graphitic architecture, doped with single nitrogen atoms and hexagonal boron nitride (h-BN) domains. The additional bands around 2900 cm<sup>-1</sup> and the shoulder around 3400 cm<sup>-1</sup> can be ascribed to C-H and B-OH stretching vibrations, respectively, most likely resulting from the edges and defects of the BNC sheets. The broad band at 3400 cm<sup>-1</sup> is assigned to the O-H stretching vibrations of H<sub>2</sub>O, adsorbed on the surface of the highly porous materials. Two additional observations can be made in the FTIR spectra of BNCs. First, the characteristic B-C stretching vibration at 1020 cm<sup>-1</sup> is absent. Therefore, no rearrangement at the nitrogen-bonded boron-core of [BIm<sub>4</sub>] takes place during pyrolysis. Second, the broad band at 1125 cm<sup>-1</sup>, with additional shoulders at  $1250~\text{cm}^{-1}$  and  $1085~\text{cm}^{-1}$ , is characteristic for the sp<sup>3</sup>-bonded wurtzite structure of boron nitride (w-BN). This phase is formed under high pressure and high temperature from either hexagonal or cubic boron nitride and is still not much investigated. Interestingly, with increasing pyrolysis temperature, the w-BN band becomes more pronounced, whereas the h-BN band decreases in intensity. Therefore, a phase transformation of h-BN to w-BN during material preparation can not be excluded. (Romanos et al., 2013, Portehault et al., 2010, Chrenko, 1974, Zhang and Meng, 2019)



**Fig. 4.** XP N 1s (left), C 1s (mid) and B 1s (right) spectra of BNC-800 (first row), BNC-900 (second row), BNC-1000 (third row); intensity scales within one column are identical. Dominant signals related to C-N, B-N, and C-C species are marked in green, blue and grey, respectively, along with a small boron-oxide contribution (magenta); broad peaks (orange) at the high binding energy side of the N 1s and C 1s regions are due to satellite features of N and C atoms in an aromatic configuration. Close-ups of the respective spectra can be found in the ESI.

**Table 2**Composition (relative to boron) of BNC-800, BNC-900 and BNC-1000, obtained *via* elemental analysis (EA) or *via* XPS measurements; The right column shows the atomic B:N ratio of the B-N related XPS signals (blue peaks in Fig. 4).

Sample	EA composition <sup>a</sup> (total sample)	XPS composition <sup>a,b</sup> (near-surface)	B: N ratio of B-N signals <sup>c</sup>		
BNC-800	$C_{17}N_{6}B$	$C_{17}N_5B$	1: 3.5		
BNC-900	$C_{38}N_5B$	$C_{18}N_3B$	1: 2.1		
BNC-1000	$C_{32}N_3B$	$C_{33}N_3B$	1: 1.8		

<sup>&</sup>lt;sup>a</sup> normalized to boron <sup>b</sup> XPS information depth of 7-9 nm <sup>c</sup> pure h-BN would have a B: N ratio of 1: 1, higher ratios arise from N bound to C in BNCs.

The composition and bonding configuration within the near-surface region of BNCs was investigated with X-ray photoelectron spectroscopy (XPS, information depth 7-9 nm). The XP spectra (see Fig. 4) essentially reveal the same bonding situation as FTIR according to literature binding energy (BE) values. (Hao et al., 2019) Species related to B-N (B 1s 191.2 eV, N 1s 398.7 eV), C-N (C 1s 286.6 eV, N 1s 400.8 eV) and C-C (C1s 284.7 eV) bonds are present confirming our FTIR results that the BNC materials consist of carbon domains with boron and nitrogen incorporated. C-B bonds could be excluded, due to missing characteristic signals in C 1s (expected at 284.1 eV) and B 1s (expected at 190.4 eV). Only a very small amount of oxidized boron (192.6 eV, around 5-8 % B-O intensity relative to B-N) is visible at the high BE side of the B-N signal for the three BNC materials in XPS (see also Table S1). Note that boronoxygen bonds have been reported in other BNC materials prepared via pyrolysis and are a result of the oxophile nature of unsaturated boron in defects. (Portehault et al., 2010) In addition, in the here investigated samples, all N 1s and C 1s spectra reveal a broad peak shifted to higher BE (orange signal in Fig. 4) that is attributed to satellites from aromatically bound carbon and nitrogen. In comparison to the overall bulk composition as given by EA, the more surface sensitive XPS analysis (integrated signal of all peaks in Fig. 4) reveals a quite good agreement of the relative C-N-B content for BNC-800 and BNC-1000 (see Table 2). in XPS, only BNC-900 shows a higher boron content relative to carbon and nitrogen determined in EA. The last column in Table 2 shows the B: N ratio of the B-N related XPS signals (blue peaks) in Fig. 4. Due to the lack of B bound to C and due to the B: N = 1: 3.5 ratio of B-N signals, we propose that in BNC-800, mainly BN3 sites, and N at C-N sites (green peaks in Fig. 4; see also ESI Table S1) are incorporated in the carbon domains. At 900°C, nitrogen mainly from C-N sites (and to some extent also from BN3 sites) starts to burn off, converting carbon into C-C carbon as shown in the C-C peak increase (see grey peaks in Fig. 4), while the boron content remains more or less constant (see ESI Table S1). 1000°C pyrolysis releases even more nitrogen but, in comparison to 900°C, also boron as shown by the drastic decreases in N 1s and B 1s intensities, again accompanied by an increased conversion into C-C carbon. The smaller B: N=1.8 ratio of B-N signals is an indication that boron nitride configurations close to the surface are formed for BNC-1000.

#### 3.3. Dye-removal using BNCs

With these BNC material features at hand, namely a high degree of heteroatom doping, a rough nanostructure paired with high porosity, the materials prepared in this study were tested for adsorption applications. As a model pollutant, methylene blue (MB) was chosen. This compound is a representative of the widely used, and partially carcinogenic, cationic dyes. (Tan et al., 2015) The BNC materials were investigated with regards to their adsorption kinetics, *i. e.* how fast they can adsorb a pollutant. Furthermore, their adsorption capacity, *i. e.* how much pollutant can actually be taken up, was studied. Both aspects are key performance indicators for a potential application as a sorbent material.

# 3.3.1. Adsorption kinetics

A fast uptake of pollutants by the adsorbent is highly desired. Therefore, all BNCs prepared in this study were tested in time-resolved adsorption experiments. Two different concentrations of MB were investigated, a moderate  $c_0$  of 20 mg  $L^{-1}$  and a relatively high  $c_0$  of 100 mg  $L^{-1}$ . Samples were taken every 30 seconds (except for BNC-800 at  $c_0=100$  mg  $L^{-1}$  where time intervals of 1 min were used instead) and subsequently analyzed via UV/Vis. The results are depicted in Fig. 5. The first observation was that a MB concentration of 20 mg  $L^{-1}$  was too low for these experiments, as complete decolorization occurred in less than one minute. At a higher  $c_0$  of 100 mg  $L^{-1}$ , all three materials still showed very fast adsorption and saturation time was after approximately 5 min. The uptake curves can be divided in three phases, best

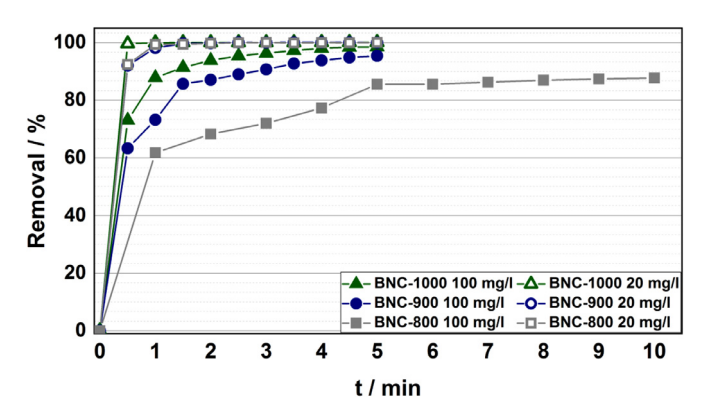


**Fig. 5.** Time resolved adsorption of MB on BNCs. 20 mg adsorbent, 50 mL MB solution,  $c_0 = 100$  mg  $L^{-1}$  (full symbols),  $c_0 = 20$  mg  $L^{-1}$  (hollow symbols), 800 rpm. Lines between data points are guidance to the eye and do not represent experimental data.

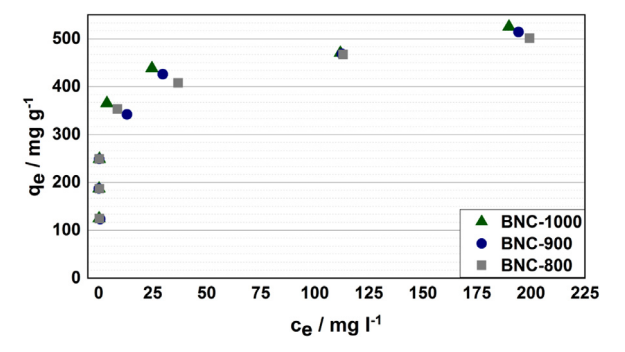


**Fig. 6.** Adsorption isotherms of MB on BNCs. 10 mg adsorbent, 25 mL of MB solution, 24 h.  $c_e$  measured with UV/Vis, calibrated at 663 nm.  $c_0$  ranging from 50 mg  $L^{-1}$  up to 400 mg  $L^{-1}$ . Experiments reproduced two times and results averaged.

seen with BNC-800. In the first phase, more than 50 % of MB is adsorbed within a few seconds, due to adsorption on the outer surface of the BNC particles. In the second phase, a linear increase in adsorption occurs, due to intra-particle transport and adsorption in the pores. In the final third phase, an adsorption-desorption equilibrium establishes. BNC-1000 displays the fastest kinetics, followed by BNC-900, and the slightly slower BNC-800. This can be explained by the rough outer surface of BNC-1000, as observed in TEM, as well as its wider micropores and higher number of mesopores, allowing for easier diffusion of MB to the adsorption sites in the particle. It is important to note that complete removal of MB (>99 % adsorbed) was achieved with our BNC-1000 material, which equals a MB take-up of 0.25 g per gram of adsorbent in only 5 min.

# 3.3.2. Adsorption capacity

The equilibrium adsorption capacity  $(q_e)$  is a measure for the amount of adsorbate an adsorbent can remove from solution in equilibrium, given in mg (pollutant) per g (adsorbent). In this study,  $q_e$  was determined in batch sorption experiments. The prepared BNCs were mixed with stock solutions of MB of varying concentration  $c_0$ . After 24 h of vigorous stirring, a sample was taken, analyzed *via* UV/Vis spectroscopy and the  $c_e$  value was calculated. The isotherm values for  $q_e$  over  $c_e$  are depicted in Fig. 6. At low concentrations of MB,  $q_e$  increases sharply for all three materials under investigation, as virtually complete decolorization of the stock solution was observed. Increasing the concentration of MB leads to the saturation of more and more adsorption sites and an adsorption-desorption equilibrium is established. The maximum adsorption capacity  $(q_{max})$  was measured with a  $c_0$  of 400 mg  $L^{-1}$  and exceeded 500 mg  $g^{-1}$  for all three BNC-materials (See ESI for a plot of  $q_e$  over  $c_0$ ).

Scheme 1. Synthesis of [EMIM][BIm<sub>4</sub>].

To the best of our knowledge, this is the highest adsorption capacity reported for MB on boron nitride or boron nitride-doped carbon-materials (see Table 3). It is an interesting fact that only small differences in q<sub>max</sub> can be observed for all three BNCs under investigation, with BNC-1000 showing approximately 10 mg  $\rm g^{-1}$  and 25 mg  $\rm g^{-1}$  higher capacity than BNC-900 and BNC-800, respectively. It is known from literature, that three factors mainly determine the adsorptive properties of nanomaterials. (El-Mahdy et al., 2020, Smith and Rodrigues, 2015, Li et al., 2018) First, a high specific surface area, because a higher surface also implies a higher number of adsorption sites. As all materials prepared in this study show very high, but slightly different specific surface areas, this factor could explain the higher  $q_{\text{max}}$  of BNC-1000. Second, sufficient pore-size, as obviously, pores smaller than the adsorbate molecule can not serve as host for the adsorption process. A higher level architecture of meso- or macropores allows for easier transport of sorbent molecules to active adsorption sites. Most pores of the BNC materials reported here are larger than the length and width of MB (14.2 Å and 5.4 Å, respectively), therefore, the pore-size of BNCs seems not to be a restricting factor. The third and most interesting factor influencing adsorptive properties is the surface functionalization of the adsorbent. MB is an organic molecule with a large aromatic ring structure, therefore  $\pi$ - $\pi$  interactions are highly relevant for adsorption. Boron nitride, as well as graphitic domains, both present in the materials studied here, provide an extensive aromatic system for  $\pi$ - $\pi$  stacking with MB, explaining the high capacity of the BNCs materials.

#### 3.3.3. Adsorption isotherm fitting

To investigate possible adsorption mechanisms and a theoretical maximum adsorption capacity, the equilibrium capacity data were non-linearly fitted with three different isotherm models, the Langmuir, the Freundlich and the Brouers-Sotolongo isotherm model (see Section 2.5 for details). To quantify the fit quality of a given model, the  $\rm R^2$  value was calculated and compared (see Table 4). Detailed graphs of the respective fits are depicted in Fig. S6a-c. According to the calculated correlation coefficient, the Langmuir isotherm model is the least suitable to describe adsorption of MB on BNCs with  $\rm R^2$  values of approximately 0.62 up to 0.92. Additionally, the  $\rm q_{max}$  predicted by this model lies below the experimental value for all three materials, implying multi-layer adsorption of MB.

The Freundlich and Brouers-Sotolongo isotherm models both show higher values for  $\mathbb{R}^2$ , ranging from approximately 0.89 to 0.93 and 0.87 to 0.96, respectively. Both models describe complex multilayer sorption on heterogeneous surfaces and both appear to accurately predict the adsorption of MB on BNCs. Interestingly, the constant  $\alpha$  in the Brouers-Sotolongo isotherm model, i. e. the measure for the energy heterogeneity of the surface, increases from BNC-800 over BNC-900 to BNC-1000. An increase in  $\alpha$  is caused by two factors. (Selmi et al., 2018) First,

**Table 3**Maximum adsorption capacity for MB on boron nitride based nanomaterials reported in literature.

Adsorbent	$q_{max} \ for \ MB \ / \ mg \ g^{-1}$	Refs.			
BNC-800	501	this study			
BNC-900	514	this study			
BNC-1000	525	this study			
Norit® CN 1 decolorizing charcoal	285 <sup>a</sup>	(FisherScientific 2020)			
Boron nitride nanosheets (BNNS)	333	(Bangari and Sinha, 2020)			
Porous BNNS	313	(Lei et al., 2013)			
h-BN	54	(Guo et al., 2019)			
h-BN	392	(Li et al., 2015)			
Porous BNNS	413 <sup>b</sup>	(Li et al., 2018)			
BN nanocarpets	272 <sup>b</sup>	(Zhang et al., 2012)			

<sup>&</sup>lt;sup>a</sup> commercial decolorizing charcoal, purchased from Acros, Lot: A0390150;

Table 4
Langmuir, Freundlich and Brouers-Sotolongo isotherm model parameters for MB adsorption on BNCs (25°C, 10 mg BNC, 25 mL MB solution). Data points nonlinearly fitted with Origin 2019.

Sample	Langmuir			Freundlich		Brouers-Sotolongo				
	q <sub>max</sub> (mg g <sup>-1</sup> )	K <sub>L</sub> (L mg <sup>-1</sup> )	R (Su et al., 2013)	$K_F$	n	R (Su et al., 2013)	q <sub>max</sub> (mg g <sup>-1</sup> )	K <sub>W</sub>	α	R (Su et al., 2013)
BNC-800	440	2.6	0.83	236.6	6.9	0.92	618	0.49	0.23	0.93
BNC-900	435	2.2	0.62	231.8	6.5	0.89	528	0.59	0.27	0.87
BNC-1000	463	3.5	0.92	261.0	7.3	0.93	508	0.79	0.32	0.96

an increase in specific surface area and widening of pores, which could already be observed in N<sub>2</sub>-sorption experiments with the BNCs under investigation. Second,  $\alpha$  increases as the surface functionality decreases. As seen in XPS analysis, BNC-800 shows the highest and BNC-1000 shows the lowest degree of B and N doping in its surface. An increase in  $\alpha$  in the adsorption experiments, therefore, agrees with the results from material characterization.

# 3.3.4. Influence of pH on adsorption

A change in the pH value of an adsorbate solution also changes the surface charge of a suspended adsorbent. As electrostatic interactions are one of the main driving forces for adsorption, the pH value is one of the key factors to tune the adsorption properties of a material. (Yu et al., 2018) BNC-1000 shows a very high capacity for MB at neutral pH, so we were interested, if at a certain pH value this property would change. A pH range from 2 to 10 with a  $c_0$  of 100 mg  $L^{-1}$  was investigated and the results are depicted in Figure S8. Note, that for these experiments a lower adsorbent loading than for the adsorption isotherm experiments was chosen, so generally, a higher  $q_{\rm e}$  can be expected.

Starting from acidic conditions, pH 2 to pH 6, BNC-1000 already shows very high capacity with 400 mg g $^{-1}$ . In neutral to basic conditions, up to pH 10, the capacity slightly increases to 416 mg g $^{-1}$ . An increase in pH beyond this point of zero charge leads to a negatively charged surface. An increase in adsorption capacity for the cationic dye MB at higher pH is therefore not surprising. Remarkably, no displacement of MB by H $^+$  occurs at low pH values, so ion-exchange and electrostatic interactions seem to play only a minor role in the adsorption on BNCs, which makes  $\pi$ - $\pi$  stacking on the aromatic surface very likely the dominant mode of interaction. Thus, BNCs have high capacity for contaminants over a very wide range of pH. This means that effective adsorption is possible independent of the acidity or basicity of the solution.

#### 4. Conclusions

The new ionic liquid  $[EMIM][BIm_4]$  was synthesized and used for the preparation of heteroatom-doped 2D carbon sheets via salt-templated pyrolysis. An increase in pyrolysis temperature led to burn-off of amor-

phous domains and gave more crystalline but turbostratic materials with high specific surface areas of up to  $1860 \, \mathrm{m^2} \, \mathrm{g^{-1}}$ . Chemical analyses showed a high degree of heteroatom-doping with isolated nitrogen atoms and boron nitride domains incorporated into the graphitic material structure. With the prepared nanomaterials the adsorption of the industrial dye methylene blue from wastewater was investigated. Decolorization of even concentrated stock solutions was observed in less than 5 minutes, and with over 500 mg g<sup>-1</sup>, the highest adsorption capacity reported so far for this class of materials was observed. Our results reveal that BNC sheets prepared from new  $[\mathrm{BIm_4}]^-$  ionic liquids are highly promising candidates for applications in technical adsorption. Moreover, we anticipate that their structural properties will also make them very interesting for the use as catalysts or catalyst supports.

# Conflicts of interest

There are no conflicts to declare.

# Notes and references

 $\dagger$ Powdered Na[BH<sub>4</sub>], as opposed to the granular form used here, leads to a sudden and violent formation of large volumes of the gaseous by-product H<sub>2</sub> and should therefore be avoided.

#### Acknowledgements

The authors like to acknowledge support by the Deutsche Forschungsgemeinschaft (DFG, German Research Foundation) in the frame of the SPP 1708 (Project-ID 237028221) and SFB 1452 (Project-ID 431791331).

#### Supplementary materials

Supplementary material associated with this article can be found, in the online version, at doi:10.1016/j.jil.2021.100004.

#### References

Titirici, M.-M., White, R.J., Brun, N., Budarin, V.L., Su, D.S., del Monte, F., Clark, J.H., MacLachlan, M.J., 2015. Chem. Soc. Rev. 44, 250–290.

 $<sup>^{\</sup>rm b}$  values obtained from the Langmuir adsorption isotherm, no experimental values for  $q_{\rm max}$  were reported in the original publications.

- Su, D.S., Perathoner, S., Centi, G., 2013. Chem. Rev. 113, 5782-5816.
- Zhao, S., Wang, D.-W., Amal, R., Dai, L., 2019, Adv. Mater. 31, 1801526.
- Jariwala, D., Sangwan, V.K., Lauhon, L.J., Marks, T.J., Hersam, M.C., 2013. Chem. Soc. Rev. 42, 2824–2860.
- Liang, C., Li, Z., Dai, S., 2008. Angew. Chem. Int. Ed. 47, 3696-3717.
- Pacuła, A., Uosaki, K., Socha, R.P., Bielańska, E., Pietrzyk, P., Zimowska, M., 2016. Electrochim. Acta 212, 47–58.
- Mombeshora, E.T., Jarvis, A.L.L., Ndungu, P.G., Doyle, B.P., Carleschi, E., Nyamori, V.O., 2017. Mater. Chem. Phys. 199, 435–453.
- Yao, Y., Zhang, B., Shi, J., Yang, Q., 2015. ACS Appl. Mater. Interfaces 7, 7413–7420. Paraknowitsch, J.P., Thomas, A., Schmidt, J., 2011. Chem. Commun. 47, 8283–8285.
- Luo, Y., Yang, Z., Guo, W., Chen, H., Wang, T., Liu, Y., Lyu, Y., Luo, H., Dai, S., 2020. J. Mater. Chem. A 8, 4740–4746.
- Yang, S.J., Rothe, R., Kirchhecker, S., Esposito, D., Antonietti, M., Gojzewski, H., Fechler, N., 2015. Carbon 94, 641–645.
- Chaudhari, K.N., Song, M.Y., Yu, J.-S., 2014. Small 10, 2625–2636.
- Gao, L., Li, R., Sui, X., Li, R., Chen, C., Chen, Q., 2014. Environ. Sci. Technol. 48, 10191–10197.
- Paraknowitsch, J.P., Thomas, A., 2012. Macromol. Chem. Phys. 213, 1132-1145.
- Zhang, S., Dokko, K., Watanabe, M., 2015. Mater. Horiz. 2, 168–197.
- Wang, X., Dai, S., 2010. Angew. Chem. Int. Ed. 49, 6664-6668.
- Chen, A., Yu, Y., Lv, H., Wang, Y., Shen, S., Hu, Y., Li, B., Zhang, Y., Zhang, J., 2013. J. Mater. Chem. A 1, 1045–1047.
- Zhang, S., Zhang, J., Zhang, Y., Deng, Y., 2017. Chem. Rev. 117, 6755–6833.
- Fellinger, T.-P., Su, D.S., Engenhorst, M., Gautam, D., Schlögl, R., Antonietti, M., 2012. J. Mater. Chem. 22, 23996–24005.
- Lee, J.S., Wang, X., Luo, H., Baker, G.A., Dai, S., 2009. J. Am. Chem. Soc. 131, 4596–4597. Prechtl, M.H.G., Scholten, J.D., Dupont, J., 2009. J. Mol. Catal. A Chem. 313, 74–78.
- Drab, D.M., Kelley, S.P., Shamshina, J.L., Smiglak, M., Cojocaru, O.A., Gurau, G., Rogers, R.D., 2012. Sci. China Chem. 55, 1683–1687.
- Kuzmina, O., Hassan, N.H., Patel, L., Ashworth, C., Bakis, E., White, A.J.P., Hunt, P.A., Welton, T., 2017. Dalton Trans. 46, 12185–12200.
- Zhu, X., Hillesheim, P.C., Mahurin, S.M., Wang, C., Tian, C., Brown, S., Luo, H., Veith, G.M., Han, K.S., Hagaman, E.W., Liu, H., Dai, S., 2012. ChemSusChem 5, 1912–1917.
- Paraknowitsch, J.P., Zhang, J., Su, D., Thomas, A., Antonietti, M., 2010. Adv. Mater. 22, 87–92.
- She, Y., Lu, Z., Ni, M., Li, L., Leung, M.K.H., 2015. ACS Appl. Mater. Interfaces 7, 7214–7221.
- Jeong, J.H., Lee, J.S., Roh, K.C., Kim, K.-B., 2017. Nanoscale 9, 14672–14681.
- Paraknowitsch, J.P., Zhang, Y., Wienert, B., Thomas, A., 2013. Chem. Commun. 49, 1208–1210.
- Panchakarla, L.S., Subrahmanyam, K.S., Saha, S.K., Govindaraj, A., Krishnamurthy, H.R., Waghmare, U.V., Rao, C.N.R., 2009. Adv. Mater. 21, 4726–4730.
- Inagaki, M., Toyoda, M., Soneda, Y., Morishita, T., 2018. Carbon 132, 104–140.
- Abbas, Q., Raza, R., Shabbir, I., Olabi, A.G., 2019. J. Sci.: Adv. Mater. Devices 4, 341–352. Gouse Peera, S., Kwon, H.-J., Lee, T.G., Hussain, A.M., 2020. Ionics 26, 1563–1589.
- Han, R., Liu, F., Wang, X., Huang, M., Li, W., Yamauchi, Y., Sun, X., Huang, Z., 2020. J. Mater. Chem. A 8, 14384–14399.
- Chen, Y., Fu, L., Liu, Z., Wang, Y., 2016. ChemCatChem 8, 1782–1787.
- Ohtani, H., Ishimura, S., Kumai, M., 2008. Anal. Sci. 24, 1335-1340.
- Paraknowitsch, J.P., Thomas, A., 2017. Chem. Synth. Appl. Graphene Carbon Mater. 21– 42. doi:10.1002/9783527648160.ch2.
- Fulvio, P.F., Lee, J.S., Mayes, R.T., Wang, X., Mahurin, S.M., Dai, S., 2011. PCCP 13, 13486–13491.
- Aijaz, A., Akita, T., Yang, H., Xu, Q., 2014. Chem. Commun. 50, 6498-6501.
- Ranjbar Sahraie, N., Paraknowitsch, J.P., Göbel, C., Thomas, A., Strasser, P., 2014. J. Am. Chem. Soc. 136, 14486–14497.
- 'SciFinder®. The choice for chemistry research™. https://scifinder.cas.org. 2021
  Bernhardt, E., Finze, M., Willner, H., 2003. Zeitschrift für anorganische und allgemeine Chemie 629, 1229–1234.

- Zhang, J., Wu, T., Feng, P., Bu, X., 2010. Dalton Trans. 39, 1702-1704.
- Galvelis, R., Slater, B., Cheetham, A.K., Mellot-Draznieks, C., 2012. CrystEngComm 14, 374–378.
- Zheng, S., Wu, T., Zhang, J., Chow, M., Nieto, R.A., Feng, P., Bu, X., 2010. Angew. Chem. Int. Ed. 49, 5362–5366.
- Chao, S., Moore, C.E., 1978. Anal. Chim. Acta 100, 457-467.
- Hamilton, B.H., Kelly, K.A., Malasi, W., Ziegler, C.J., 2003. Inorg. Chem. 42, 3067–3073. Fechler, N., Fellinger, T.-P., Antonietti, M., 2013. Adv. Mater. 25, 75–79.
- Niedermaier, I., Kolbeck, C., Steinrück, H.-P., Maier, F., 2016. Rev. Sci. Instrum. 87, 045105
- Langmuir, I., 1918. J. Am. Chem. Soc. 40, 1361-1403.
- Freundlich, H., 1907. Zeitschrift für Physikalische Chemie 57U, 385-470.
- Brouers, F., Sotolongo, O., Marquez, F., Pirard, J.P., 2005. Physica A 349, 271–282.
- Ncibi, M.C., Altenor, S., Seffen, M., Brouers, F., Gaspard, S., 2008. Chem. Eng. J. 145, 196–202
- Altenor, S., Carene, B., Emmanuel, E., Lambert, J., Ehrhardt, J.-J., Gaspard, S., 2009. J. Hazard. Mater. 165, 1029–1039.
- Fechler, N., Tiruye, G.A., Marcilla, R., Antonietti, M., 2014. RSC Adv. 4, 26981–26989.
- Castro-Muñiz, A., Nishihara, H., Hirota, T., Ohwada, M., Li, L.-X., Tsuda, T., Kuwabata, S., Maruyama, J., Kyotani, T., 2017. Chem. Commun. 53, 13348–13351.
- Rao, C.N.R., Sood, A.K., Subrahmanyam, K.S., Govindaraj, A., 2009. Angew. Chem. Int. Ed. 48, 7752–7777.
- Thommes, M., Kaneko, K., Neimark, A.V., Olivier, J.P., Rodriguez-Reinoso, F., Rouquerol, J., Sing, K.S.W., 2015. Pure Appl. Chem. 87, 1051–1069.
- Lazzarini, A., Piovano, A., Pellegrini, R., Agostini, G., Rudić, S., Lamberti, C., Groppo, E., 2016. Physics Procedia 85, 20–26.
- Tuinstra, F., Koenig, J.L., 1970. J. Chem. Phys. 53, 1126-1130.
- Ferrari, A.C., Robertson, J., 2000. Phys. Rev. B 61, 14095-14107.
- Romanos, J., Beckner, M., Stalla, D., Tekeei, A., Suppes, G., Jalisatgi, S., Lee, M., Hawthorne, F., Robertson, J.D., Firlej, L., Kuchta, B., Wexler, C., Yu, P., Pfeifer, P., 2013. Carbon 54, 208–214.
- Portehault, D., Giordano, C., Gervais, C., Senkovska, I., Kaskel, S., Sanchez, C., Antonietti, M., 2010. Adv. Funct. Mater. 20, 1827–1833.
- Chrenko, R.M., 1974. Solid State Commun. 14, 511-515.
- Zhang, X., Meng, J., 2019. Ultra-Wide Bandgap Semiconductor Materials. Elsevier, pp. 347–419. doi:10.1016/B978-0-12-815468-7.00004-4 eds. M. Liao, B. Shen and Z. Wang.
- Hao, Q., Song, Y., Mo, Z., Mishra, S., Pang, J., Liu, Y., Lian, J., Wu, J., Yuan, S., Xu, H., Li, H., 2019. ACS Sustainable Chem. Eng. 7, 3234–3242.
- Tan, K.B., Vakili, M., Horri, B.A., Poh, P.E., Abdullah, A.Z., Salamatinia, B., 2015. Sep. Purif. Technol. 150, 229–242.
- El-Mahdy, A.F.M., Zakaria, M.B., Wang, H.-X., Chen, T., 2020. Y. Yamauchi and S.-W. Kuo. J. Mater. Chem. A doi:10.1039/D0TA07281H.
- Smith, S.C., Rodrigues, D.F., 2015. Carbon 91, 122–143.
- Li, L., Sun, F., Gao, J., Wang, L., Pi, X., Zhao, G., 2018. RSC Adv. 8, 14488-14499.
- FisherScientific, https://www.fishersci.com/shop/products/carbon-activated-norit-cn-acros-organics-2/AC404042500, accessed November 2020.
- Bangari, R.S., Sinha, N., 2020. J. Nanosci. Nanotechnol. 20, 6222-6234.
- Lei, W., Portehault, D., Liu, D., Qin, S., Chen, Y., 2013. Nat. Commun. 4, 1777.
- Guo, Y., Wang, R., Wang, P., Rao, L., Wang, C., 2019. ACS Sustainable Chem. Eng. 7, 5727–5741.
- Li, J., Huang, Y., Liu, Z., Zhang, J., Liu, X., Luo, H., Ma, Y., Xu, X., Lu, Y., Lin, J., Zou, J., Tang, C., 2015. J. Mater. Chem. A 3, 8185–8193.
- Li, J., He, S., Li, R., Dai, W., Tao, J., Wang, C., Liu, J., Wu, T., Tang, C., 2018. RSC Adv. 8, 32886–32892.
- Zhang, X., Lian, G., Zhang, S., Cui, D., Wang, Q., 2012. CrystEngComm 14, 4670–4676. Selmi, T., Seffen, M., Sammouda, H., Mathieu, S., Jagiello, J., Celzard, A., Fierro, V., 2018. Adsorption 24, 11–27.
- Yu, S., Wang, X., Pang, H., Zhang, R., Song, W., Fu, D., Hayat, T., Wang, X., 2018. Chem. Eng. J. 333, 343–360.